Next-to-leading-order terms for the brighter/fatter effect in thick CCDs: Are perturbations linear over 3 orders of magnitude?

Andy Rasmussen, SLAC National Accelerator Lab ISPA Pasadena, 181203-4

Abstract: To do a better job[0] with instrument signature removal (ISR) in the ubiquitous devices subject to the brighter-fatter effect (BF), we extend a previously developed[1] framework for estimating LSST CCD sensor electrostatic parameters[2] using available diagnostic data[3]. The new functionality provides tabulation of specific pixel boundary overlap areas between undistorted, nominal pixel domains and adjacent pixel domains distorted by an electrostatic aggressor. When evaluating these overlap areas over the entire sensor dynamic range[4], we note significant (several percent level) deviations from the constant overlap area derivative with respect to aggressor signal. This suggests limited usefulness of a constant brighter-fatter kernel if we indeed would like to use the highest SNR, otherwise clean PSF estimators across the field.

We therefore propose a 5-index, sparse differential overlap matrix $M_{iji'j'k}$ to encapsulate and convey drift calculation results as a drop-in replacement ISR data product for sequential, successive-over-relaxation (SOR) methods to map recorded signal distributions onto an incident flux distribution estimate. This would remove untested symmetry assumptions of the boundary displacement kernel, e.g., that the boundary displacement may be expressed as the gradient of a scalar field.

Existing framework for fitting lag-specific patterns of flat field correlations to estimate electrostatic parameters

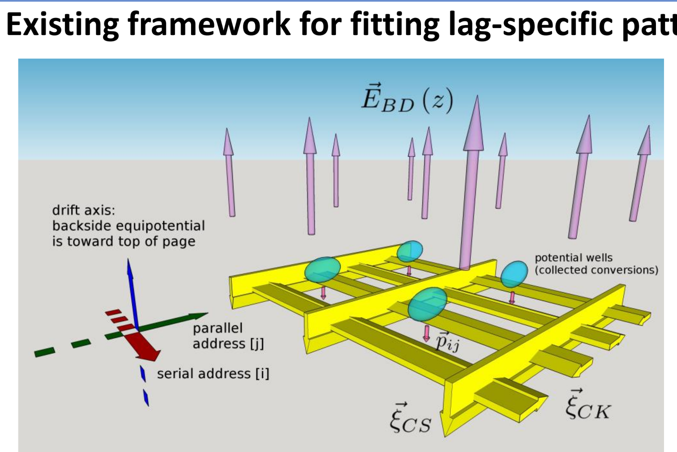

Cartoon of assumed drift field contributions

$$\mathrm{A}_{ij} \equiv +\frac{1}{2}\sum_{k=0}^{N-1}(x_{k+1}y_k - x_k y_{k+1});$$

$$\mathrm{Ixx}_{ij}\mathrm{A}_{ij} \equiv -\frac{1}{12}\sum_{k=0}^{N-1}(y_{k+1}-y_k)(x_k^2+x_{k+1}^2)(x_k+x_{k+1});$$

$$\mathrm{Iyy}_{ij}\mathrm{A}_{ij} \equiv +\frac{1}{12}\sum_{k=0}^{N-1}(x_{k+1}-x_k)(y_k^2+y_{k+1}^2)(y_k+y_{k+1});$$

$$\mathrm{Ixy}_{ij}\mathrm{A}_{ij} \equiv +\frac{1}{6}\sum_{k=0}^{N-1}(x_{k+1}-x_k)x_k(y_k^2+y_{k+1}^2+y_k y_{k+1}) + \frac{1}{24}\sum_{k=0}^{N-1}(x_{k+1}-x_k)^2(y_k^2+3y_{k+1}^2+2y_k y_{k+1});$$

$$\mathrm{Ix}_{ij}\mathrm{A}_{ij} \equiv -\frac{1}{6}\sum_{k=0}^{N-1}(y_{k+1}-y_k)(x_k^2+x_{k+1}^2+x_k x_{k+1});$$

$$\mathrm{Iy}_{ij}\mathrm{A}_{ij} \equiv +\frac{1}{6}\sum_{k=0}^{N-1}(x_{k+1}-x_k)(y_k^2+y_{k+1}^2+y_k y_{k+1}).$$

Shoelace formulae that connect pixel boundaries to relevant geometry

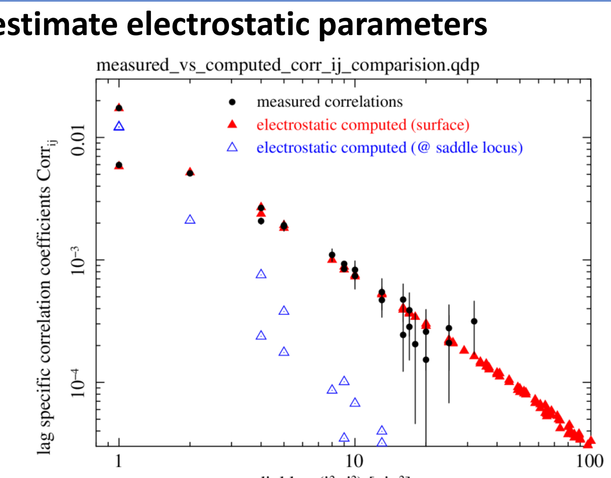

Comparison of best fit drift model to measured flat field correlations

Table 1. Parameter list for the best-fit electrostatic drift model (for cold carriers)

parameter	value	units	comments
N_a	1.11×10^{12}	cm^{-3}	acceptor density in depleted Si
t_{Si}	100	μm	sensor thickness (fixed)
BSS	-78	Volts	backside bias (fixed)[a]
ξ_{cs}	12.407	ξ_0[b]	channel stop 2-D dipole moment
ξ_{ck}	2.6425	ξ_0[b]	clock barrier 2-D dipole moment
$\bar{p}$	0.0057208	p_0[c]	aggressor dipole moment[d]
μ	65230	e^-	mean signal level in flat
ζ^2	58429	$(e^-)^2$	variance in flat[d]

[a] constrained by measured X-ray diffusion variation with BSS on a similar device
[b] $\xi_0 \equiv 10^{-6}\, q_e$
[c] $p_0 \equiv 10^5\, \mu m\, q_e$
[d] exposure averaged, *rms* aggressor moment is $\bar{p} \equiv z_{chan}\, \zeta\, q_e$

The best fit parameters for the observed flat field correlation pattern

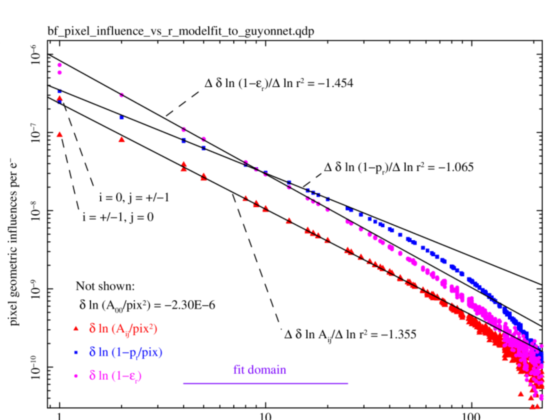

Per-electron geometric influences induced by collected conversions

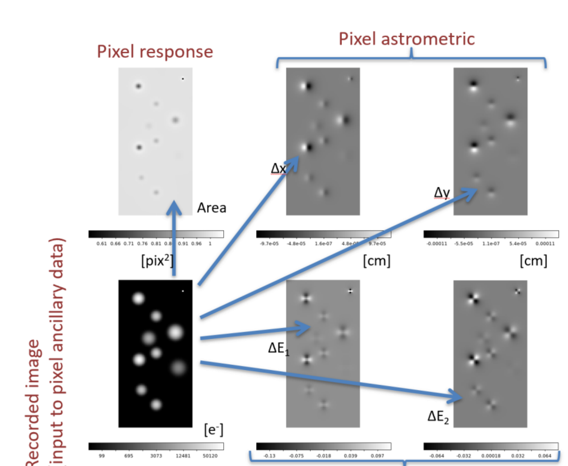

Exposure-averaged pixel geometry perturbation maps for a specific recorded image (better background correction, better moments)

Computed evolution of pixel boundaries as aggressor approaches the nominal full well depth of 100ke-

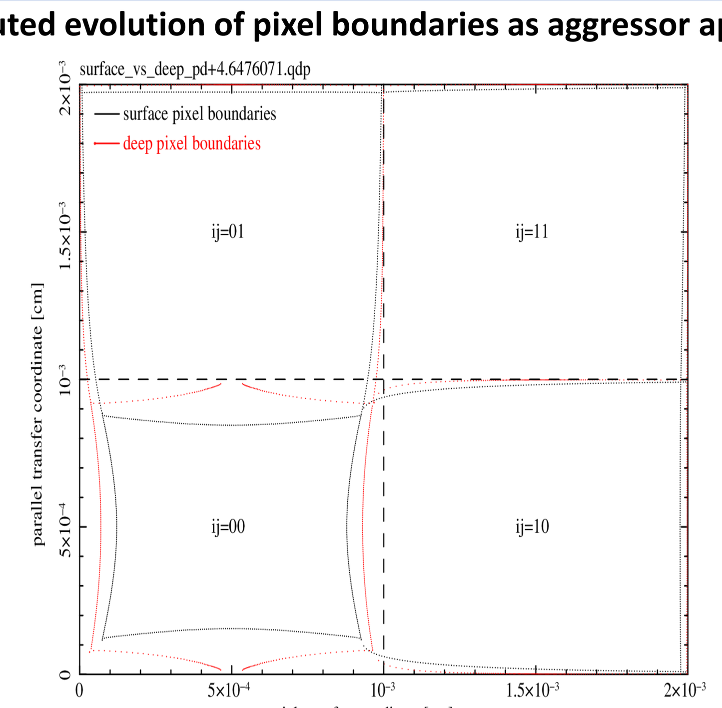

Cold carrier pixel boundaries evaluated at the surface (black) and at the deep saddle locus (red). Chromatic dependence is apparent.

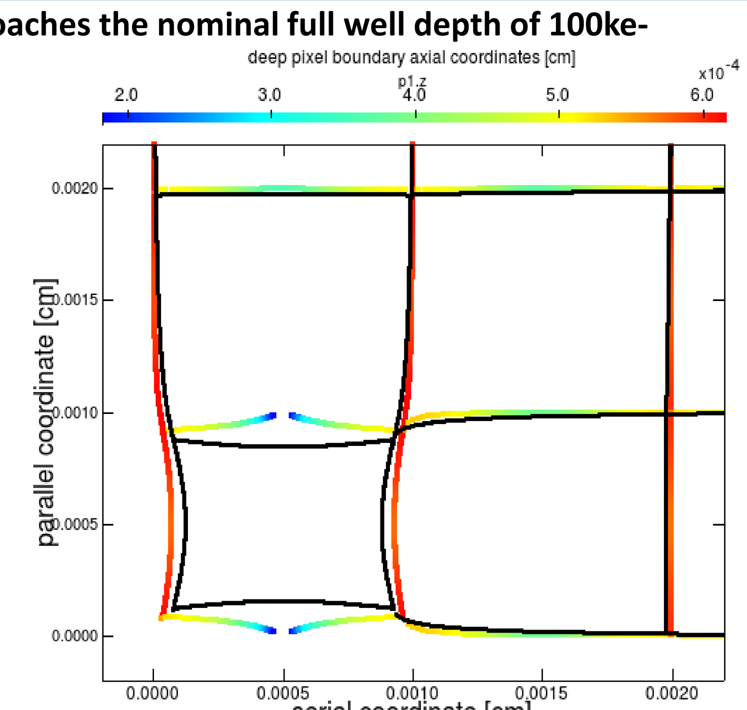

Variation in axial coordinate of saddle locus may help to explain generic measurement results that show $I_{XX} < I_{YY}$ for X-rays and high quality spots.

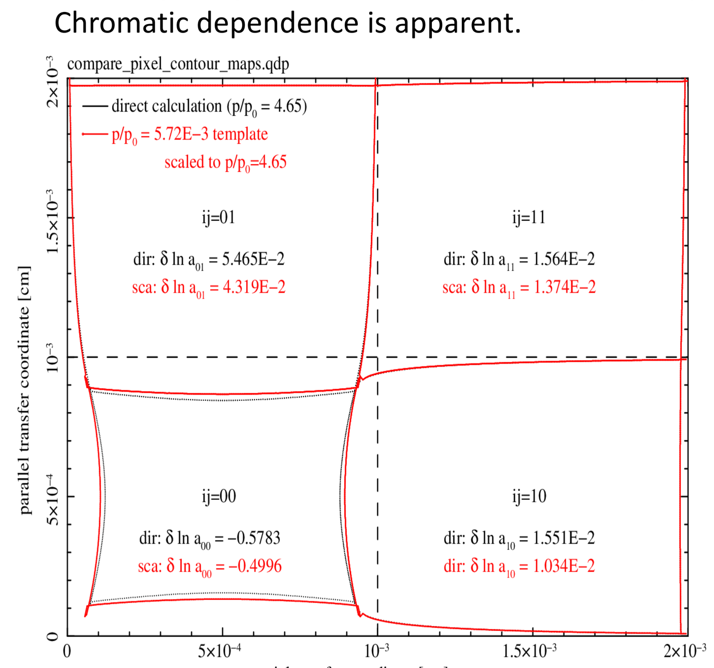

Direct calculation results for full well aggressors differ sufficiently (typ. 10%) from pixel geometry derived from scaled, detailed boundary distortion templates which are in turn a byproduct of fitting to measured flat field correlations. In this case, the effective aggressor driving correlations are about 1/800 of the full well. This was realized in a previous publication and we began to pursue a "stack strategy" for BF kernels, (indexed by aggressor amplitude) in place of the approach that uses a single kernel, inferred only from flat field pair difference correlations.

Pixel overlap polygons are required to properly redistribute recorded signal

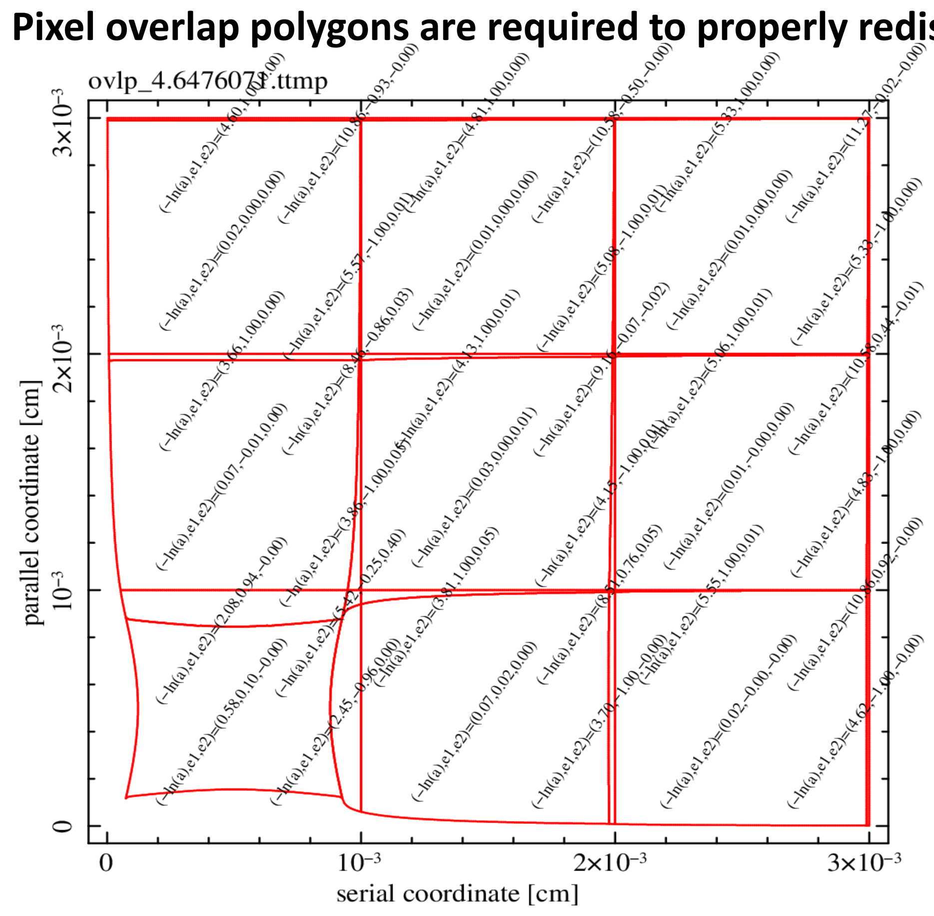

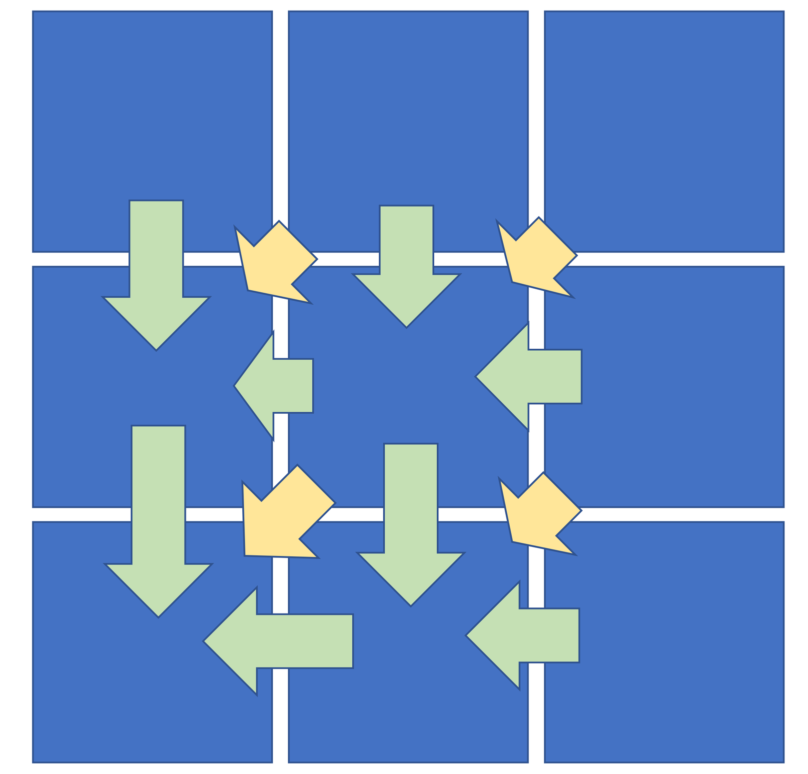

Left: A quantitative tabulation of overlap areas, representing integrals over a slice of the differential overlap matrix: $A_{iji'j'}(Q_{00}) = \int_0^{Q_{00}} dq_{00} \frac{dk}{dq_{00}} M_{iji'j'k}$. Right: a cartoon of the signal redistribution that reassembles an estimate for the incident flux distribution from the recorded signal distribution, limited to the first 12 terms that redistribute into the leading 4 pixels. Overlap areas represented by green arrows are expected to scale mostly linearly with aggressor signal (and with local flux), whereas yellow arrows are expected to scale mostly quadratically.

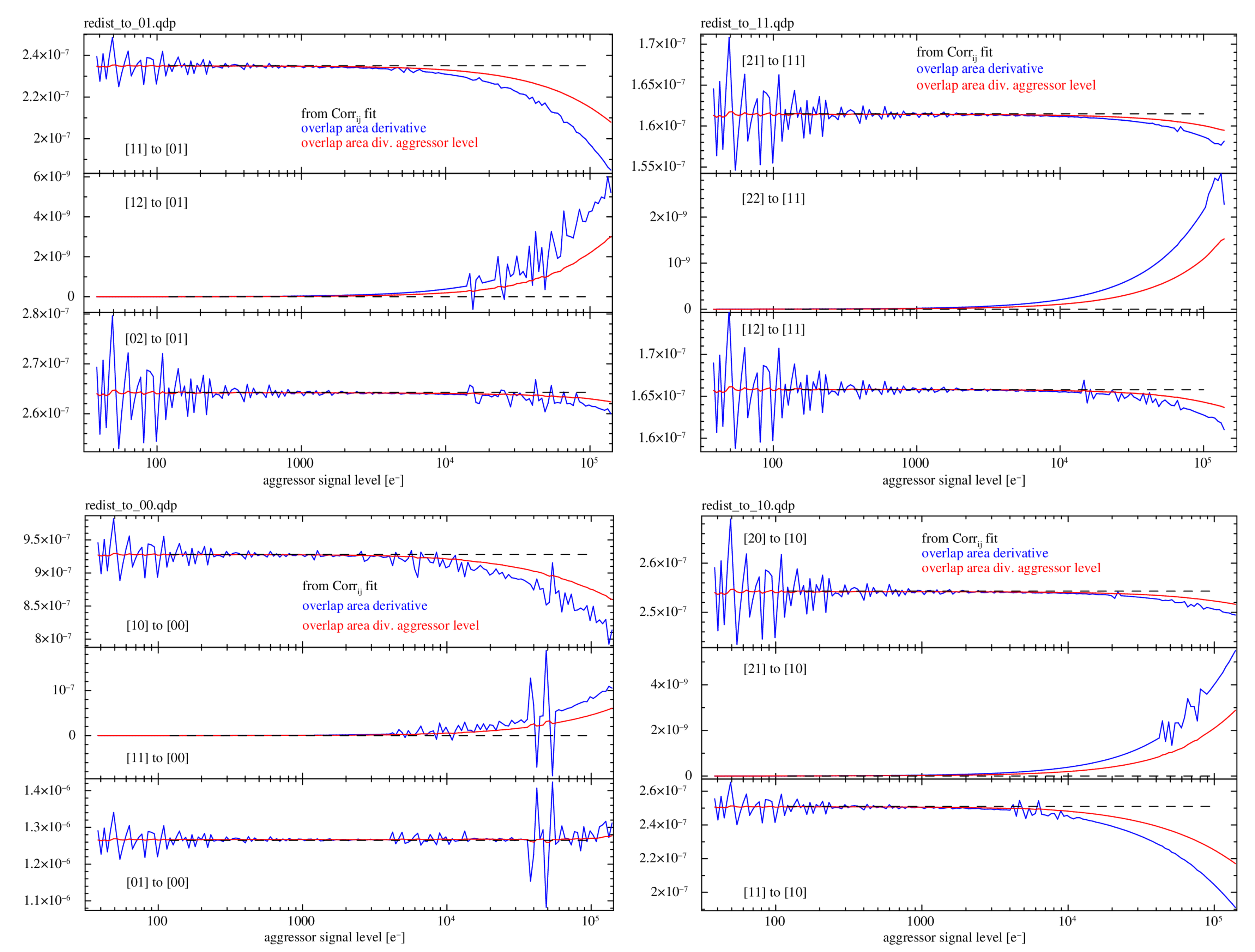

Above: Blue curves are the overlap area derivative matrix elements $M_{iji'j'k}$ for lags $[ij] = [00], [10], [01]$ & $[11]$ for the 3 feeding neighbors with lags $[i'j'] = [ij] + [10], [11]$ & $[01]$. We compare the area derivatives against the flat field correlation inferred overlap derivatives (dashed lines) and against overlap area-to-aggressor ratios (red curves). The mismatch between exposure averaged overlap area derivatives and instantaneous overlap area derivatives underscore where the constant signal displacement kernel correction is partial – typically near 10% of full well.

Discussion: sensors expressing a 10% sag (or missing variance) in their mean-variance relations near FW also apparently show a 90% maximum ISR completeness near FW, based on the various methods employed to date. *This might not be a coincidence!* The current limitation might simply be due to the fact that pixel area distortions are easily measured only up to aggressor levels of $q_{max} \sim \sqrt{FW}/2$ whereas we've shown here that most deviations from linear occur in the interval [0.1, 1] times FW – a required dynamic range factor of 800 in the case demonstrated here. Ideas are more than welcome for how we can probe the top 90% register for this purpose. High contrast fringe + flat field projectors (w/swappable illumination order) continue to hold promise. We plan to package up these inter-lag overlap area derivatives in a form that should be useful for validating pipeline implementation of this finer granularity ISR approach. Revisiting our Monte Carlo generated incident and recorded image pairs will be a logical first step.

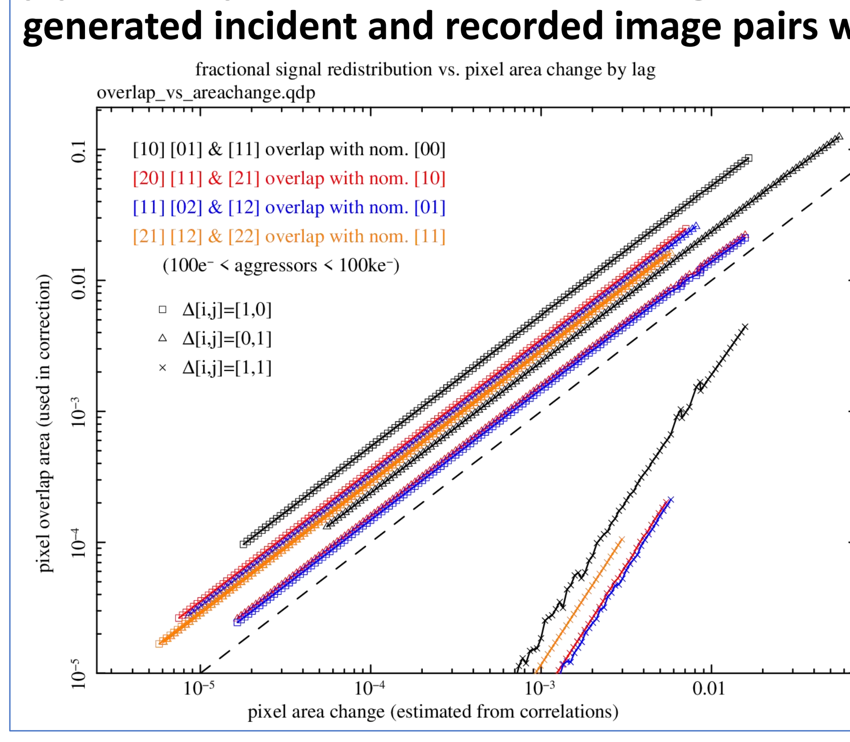

A representation of the proximal 12 terms in the measured BF effect, evaluated over the 3 orders of magnitude in aggressor amplitude – correction over which would provide full utilization the sensor's dynamic range. For each inter-lag overlap, the instantaneous overlap area is plotted along the vertical axis and arranged horizontally by the ***debtor*** pixel's instantaneous area excess. Area excesses (the horizontal axis) are simply related to flat field correlations. Deriving the inter-lag overlaps either requires a large number of lag-specific correlation values, some assumed properties of the pixel boundary displacement field, or (in this case) a relatively coherent drift model that can reproduce available diagnostic data.

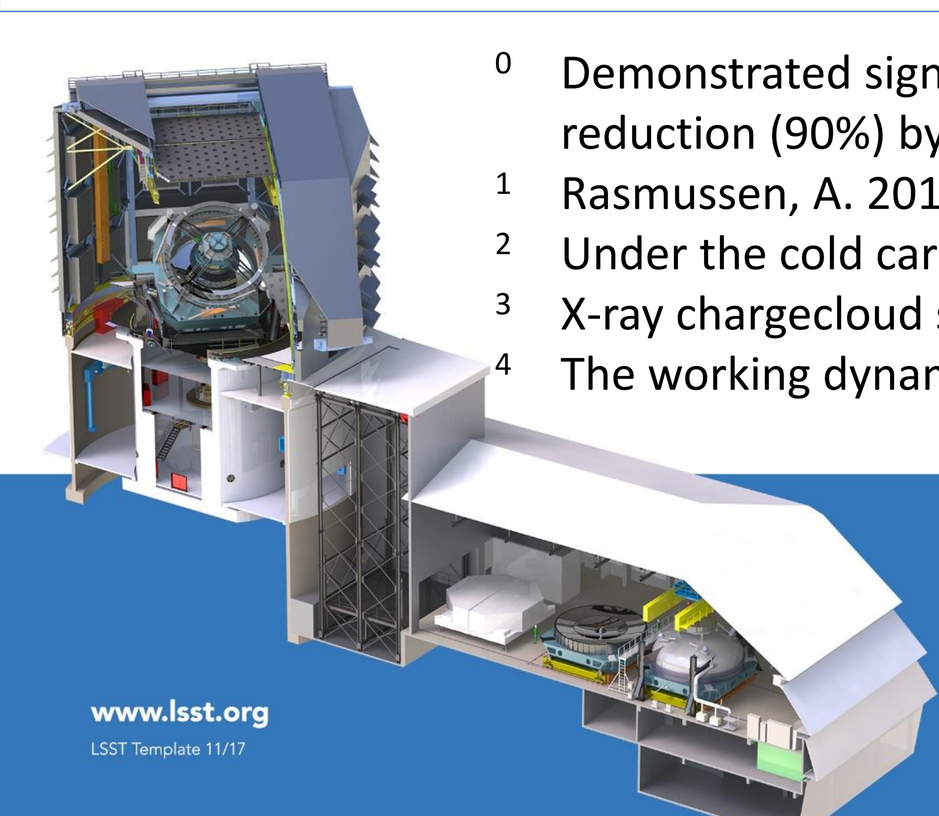

[0] Demonstrated signal redistribution algorithms (Antilogus et al. 2014, Gruen et al. 2015, Guyonnet et al. 2015, Coulton et al. 2018) provide incomplete reduction (90%) by redistributing fractional signal between specific lags according to the pixel boundary shift hypothesis.
[1] Rasmussen, A. 2014, **JINST 10**, 05, C05028 (arXiv:1502.02751), Rasmussen, A. et al., 2016, **Proc. SPIE 9915**, 99151A (arXiv:1608.01964).
[2] Under the cold carrier assumption.
[3] X-ray chargecloud sum ratios and lag-specific correlations extracted from flat field pair difference images.
[4] The working dynamic range we consider spans the integration-time averaged statistical fluctuations (120e-) through the required full well depth of 100ke-

This material is based upon work supported in part by the National Science Foundation through Cooperative Support Agreement (CSA) Award No. AST-1227061 under Governing Co-operative Agreement 1258333 managed by the Association of Universities for Research in Astronomy (AURA), and the Department of Energy under Contract No. DE-AC02-76SF00515 with the SLAC National Accelerator Laboratory. Additional LSST funding comes from private donations, grants to universities, and in-kind support from LSSTC Institutional Members.